APS physics

CHORUS

This is the accepted manuscript made available via CHORUS. The article has been published as:

Localized nonlinear edge states in honeycomb lattices

Mark J. Ablowitz, Christopher W. Curtis, and Yi Zhu

Phys. Rev. A **88**, 013850 — Published 29 July 2013

DOI: 10.1103/PhysRevA.88.013850

Localized Nonlinear Edge States in Honeycomb Lattices

Mark J. Ablowitz and Christopher W. Curtis
Department of Applied Mathematics, University of Colorado, Boulder, Colorado 80309, USA

Yi Zhu
Zhou Pei-Yuan Center for Applied Mathematics, Tsinghua University, Beijing 100084, China

Two-dimensional localized edge modes in optical honeycomb lattices are found and analyzed analytically and computationally. Weak nonlinearity and transverse modulation are found to introduce self-phase modulation in the phase and create internal nonlinear interactions as the electromagnetic field propagates through the lattice. Even with relatively strong nonlinearity localization and persistence of modes along the edge is found.

I. INTRODUCTION

An interesting class of optical media are two-dimensional-waveguide arrays, or photonic lattices, where the material of the array has a significant nonlinear response in the presence of high intensity fields. Researchers have observed in photonic lattices the formation of localized waves, or solitons, which exhibit stable propagation in both one and two dimensional lattices. This includes discrete solitons [1], dipole solitons [2], vortex solitons [3] and soliton-trains [4]. It has been found that periodic as well as more complex quasi-periodic lattice backgrounds, *cf.* [5] and [6], can admit a wide variety of stable nonlinear modes.

However, the periodic lattices used in the previous cases were simple periodic lattices. A less well studied and understood media, but one of growing importance, is a photonic lattice with a honeycomb (HC) periodic structure. Due to both their geometry and increasing importance, honeycomb photonic lattices are commonly called "optical graphene". Researchers have observed such phenomena as conical diffraction [7, 8], band gap-solitons [9], and pseudo-magnetic response at optical frequencies [10] in honeycomb lattices.

The novel phenomena in optical graphene is due to the existence of Dirac points, which are points in the Brillouin zone at which the dispersion bands meet in intersecting cones. The conical intersection means the bands have infinite curvature at the Dirac points, which, in solid-state systems leads to zero effective mass and near-relativistic dynamics. This striking common feature between optical and solid state systems has motivated researchers to explore what features present in carbon based graphene can be found in the optical equivalent.

A related topic of considerable current research is the effects of introducing interfaces into a photonic lattice. In this case, researchers have studied the formation of edge states in honeycomb lattice systems. Importantly, in certain cases edge states have been found to exhibit stable, localized, uni-directional propagation of motion [11] with limited backscatter. While traditionally studied in the context of condensed-matter physics [12–15], the appearance of edge states in optical graphene has recently been experimentally observed in [16]. Further, it has been shown that edge states can exist in strained and compressed optical lattices [10, 17]. Interesting recent research also include theoretical studies [18–20] and experimental observation [21] of topologically-protected optical edge states in special types of honeycomb lattices.

The above research, however, involves edge states modeled by strictly linear systems where the edge states represent the ground state energy, or zero energy, modes. Edge states in one-dimensional nonlinear lattices have been studied in [22], and in [23], numerically constructed, excited energy edge states are found for honeycomb photonic lattices. However, to our knowledge, the effects of nonlinearity on the class of zero-energy edge modes have not been analyzed. Further, previous theoretical results on linear systems found edge modes via Fourier transforms at a particular frequency; hence these edge modes represent monochromatic plane waves oscillating in the direction parallel to the edge.

Given the significant role that nonlinearity plays in many optical systems, and the added structure of the two-dimensional honeycomb lattice, it is a natural question to explore the impact of these effects on an important class of physical phenomena. Thus in this paper, we examine the how Kerr type nonlinearities modify the propagation of two dimensional linear, ground state edge modes. One of the questions we address is whether nonlinearity plays a significant role in delocalizing two-dimensional edge modes away from the edge by causing them to scatter into the bulk of the lattice.

To generate these two-dimensional localized edge modes, we modulate the monochromatic edge modes in the spatial direction parallel to the edge; this allows us to construct fully localized wave packets. We find there is an important interplay between nonlinearity and the modulation of the edge modes. To describe this balance, we construct a *slowly-modulated-wave packet*, which is a two dimensional wave packet with weak modulation in the direction parallel to the edge. The effect of weak nonlinearity on slowly-modulated-wave packets is to introduce a *self-phase modulation* of the zero-energy linear solution. This preserves localization of the mode along the edge. We then show via numerical simulations that localization is largely preserved even as the nonlinearity and transverse modulation are suitably increased.

A. Physical Model

The propagation of an electromagnetic field in a two dimensional, honeycomb lattice with nonlinear interactions may be described via the following normalized nonlinear Schrödinger equation with periodic potential,

$$i\partial_z\psi = -\Delta\psi + \frac{1}{h^2}V(x,y)\psi + \sigma|\psi|^2\psi. \tag{1}$$

Here, ψ is the normalized electric field, V is the linear periodic index of refraction, h is the strength of the potential, the lattice is taken to have honeycomb structure, the coefficient $\sigma = \pm 1$ represents "normal" and "anomalous" dispersion respectively, and z is the direction of propagation.

The honeycomb structure is related to there being two minima in the index of refraction V per fundamental cell in the lattice. The nonlinearity is due to propagation through a Kerr medium. Nonlinear Schrödinger equations with potentials in the context of Bose-Einstein condensates are also referred to as Gross-Pitaevskii equations.

Taking advantage of the field's tendency to localize around minima in the index of refraction, using a tight-binding nearest neighbor approximation, *cf.* [24], in the limit as $h \to 0$ produces a nonlinear lattice system of the form

$$i\frac{dA_{mn}(z)}{dz} + (\mathcal{L}_-\mathbf{B})_{mn} + \tilde{\sigma}|A_{mn}|^2A_{mn} = 0, \tag{2}$$
$$i\frac{dB_{mn}(z)}{dz} + (\mathcal{L}_+\mathbf{A})_{mn} + \tilde{\sigma}|B_{mn}|^2B_{mn} = 0, \tag{3}$$

where

$$(\mathcal{L}_-\mathbf{B})_{mn} = B_{mn} + \rho e^{-i\theta_1}B_{m-1,n-1} + \rho e^{-i\theta_2}B_{m+1,n-1},$$
$$(\mathcal{L}_+\mathbf{A})_{mn} = A_{mn} + \rho e^{i\theta_1}A_{m+1,n+1} + \rho e^{i\theta_2}A_{m-1,n+1}.$$

The discrete system (2) – (3) was derived in [25]. The functions $A_{mn}(z)$ and $B_{mn}(z)$ represent the field strength at the lattice sites with A_{mn} representing the black dots, and B_{mn} representing the grey as seen in Figure 1. The functions $\mathbf{A}$ and $\mathbf{B}$ are arranged on a honeycomb lattice that shows each $\mathbf{A}$-site is surrounded by three nearest neighbors that are at $\mathbf{B}$-sites. Note, in [25], the discrete system was indexed by the period vectors of the honeycomb lattice. In this paper, we have instead indexed the lattice in a *row/column* format, where m denotes the row and n the column; see Figure 1 for reference. We describe the lattice throughout the text first as a sequence of columns, each with a sequence of rows within each column. For example, we describe the n^{th} column of $\mathbf{A}$-sites as $\mathbf{A}_n$, and then each entry of $\mathbf{A}_n$ is denoted by $\mathbf{A}_{mn}$. Details regarding the lattice can be found in the Appendix.

In (2) – (3), the values $\theta_j = \mathbf{k}\cdot\mathbf{v}_j$ are constant phases reflecting the influence of the Brillouin zone, where $\mathbf{k}$ is in the Brillouin zone and $\mathbf{v}_j$ is one of the period vectors

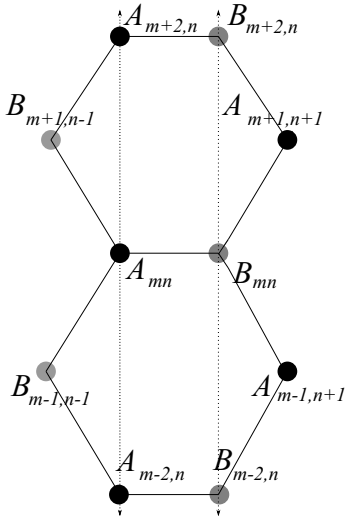

FIG. 1. Indexing scheme for honeycomb lattice with *row*(m)/*column*(n) format. The vertical bars indicate separate columns of lattice sites.

of the lattice. This is to say that taking tight-binding approximations at different places in the Brillouin zone impacts nearest-neighbor interactions between lattice sites. See [25] for more details about these terms. The effective nonlinearity $\tilde{\sigma}$ is an $\mathcal{O}(1)$ term related to σ that likewise may have either sign. The value ρ represents the amount of deformation away from a perfect hexagonal honeycomb, with $\rho = 1$ representing zero deformation. One of the interesting aspects of this discrete system is that for certain choices of θ_j corresponding to the locations of the Dirac points in the Brillouin zone, the continuum limit of the discrete system is the Dirac equation [25], which has been shown to give rise to such phenomena as conical diffraction. Various aspects of the dynamics of these equations were also studied in [25], and a detailed study of the validity of the tight-binding approximation was presented in [26].

B. Definitions and Notational Conventions

It is convenient to write the nonlinear lattice system in the compact matrix form

$$i\frac{d}{dz}\begin{pmatrix}\mathbf{A}\\ \mathbf{B}\end{pmatrix} + \begin{pmatrix}0 & \mathcal{L}_-\\ \mathcal{L}_+ & 0\end{pmatrix}\begin{pmatrix}\mathbf{A}\\ \mathbf{B}\end{pmatrix} + \tilde{\sigma}\begin{pmatrix}|\mathbf{A}|^2\mathbf{A}\\ |\mathbf{B}|^2\mathbf{B}\end{pmatrix} = 0. \tag{4}$$

Throughout the text, we use the norms

$$||\mathbf{A}||_2 = \left(\sum_{m=-\infty}^{\infty}\sum_{n=0}^{\infty}|A_{mn}|^2\right)^{1/2},$$

and

$$||\mathbf{A}||_4 = \left(\sum_{m=-\infty}^{\infty}\sum_{n=0}^{\infty}|A_{mn}|^4\right)^{1/4}.$$

We also define the phases φ_+ and φ_-

$$\varphi_+ = (\theta_2 + \theta_1)/2,\ \varphi_- = (\theta_2 - \theta_1)/2 \tag{5}$$

and the standard Fourier series basis via $e_m(\omega)$ where

$$e_m(\omega) = \frac{e^{im\omega}}{\sqrt{2\pi}}.$$

We work on the periodic interval $[-\pi+\varphi_-, \pi+\varphi_-]$, and so we point out that one has

$$\int_{-\pi+\varphi_-}^{\pi+\varphi_-} d\omega\ e_m(\omega)e_n^*(\omega) = \delta_{mn},$$

where the $*$ denotes complex conjugation and δ_{mn} is the discrete Dirac delta function.

C. Edges and Modulated-Wave Packets

In this paper, we simulate all edges by forcing the fields at the **A** and **B** sites to be zero beyond a certain column in the lattice. This can be done in several different ways which results in several different edge geometries. The two geometries that are the focus of this paper are the so called bearded and zig-zag edges, *cf.* [13]. See Figure 2 for reference. The bearded edge has all columns to the

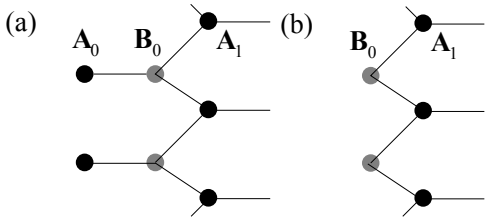

FIG. 2. In (a) we see the bearded edge, while in (b) the zig-zag edge is shown. In each figure **A** and **B** are zero to the left of the edge. $\mathbf{A}_0$ refers to the 0^{th} column of **A**-sites and $\mathbf{B}_0$ the 0^{th} column of **B**-sites.

left of the 0^{th} column set to zero. In the zig-zag edge, all columns to the left of and including $\mathbf{A}_0$, the 0^{th} column of **A**-sites, are set to zero. Here we only introduce one edge into the lattice and otherwise allow the lattice to expand infinitely.

As we discuss below, there are several differences between the two edges. The bearded edge modes are localized in the **A**-sites with the **B**-sites having vanishing field strength, while zig-zag edge modes are localized in the **B**-sites *etc...* Further, we show that the different edge cases only exist in certain frequency bands. These bands are disjoint in the two cases with the edges between the bands being determined by the Dirac points in the continuous problem (1).

For both edges though, we consider a weakly nonlinear version of (4)

$$i\frac{d}{dz}\begin{pmatrix}\mathbf{A}\\ \mathbf{B}\end{pmatrix} + \begin{pmatrix}0 & \mathcal{L}_-\\ \mathcal{L}_+ & 0\end{pmatrix}\begin{pmatrix}\mathbf{A}\\ \mathbf{B}\end{pmatrix} + \epsilon\begin{pmatrix}|\mathbf{A}|^2\mathbf{A}\\ |\mathbf{B}|^2\mathbf{B}\end{pmatrix} = 0, \tag{6}$$

where we take $0 < \epsilon \ll 1$. Note, for convenience we have replaced $\tilde{\sigma}$ by ϵ. The introduction of the small nonlinearity allows us to develop a perturbative method for studying the impact of nonlinearity. In particular, we perturb around ground state solutions; *i.e.* solutions to the steady linear problem

$$\begin{pmatrix}0 & \mathcal{L}_-\\ \mathcal{L}_+ & 0\end{pmatrix}\begin{pmatrix}\mathbf{A}\\ \mathbf{B}\end{pmatrix} = 0.$$

The solutions to this leading order problem provide, as we show, modes that are localized along the edge represented by the column $n = 0$; they are linear edge states. This approach conforms with current applications of edge states which treats nonlinearity as generally weak [16].

For the bearded case, the linear edge states that we consider are of the form

$$\begin{pmatrix}\mathbf{A}^{(env)}\\ 0\end{pmatrix},$$

where

$$\mathbf{A}^{(env)}_{mn} = \frac{1}{\sqrt{\nu}\,||\bar{\alpha}||_2}\int_{-\pi+\varphi_-}^{\pi+\varphi_-} d\omega\bar{\alpha}\left(\frac{\omega}{\nu}\right)\mathbf{a}_n^{(Nu)}(\omega)e_m(\omega). \tag{7}$$

The function $\mathbf{a}_n^{(Nu)}(\omega)$, which is derived below, see equation (14), is given by

$$\mathbf{a}_n^{(Nu)}(\omega) = \left(1 - \frac{1}{4\cos^2(\omega-\varphi_-)}\right)^{1/2}\left(\frac{e^{i(\pi-\varphi_+)}}{2\rho\cos(\omega-\varphi_-)}\right)^n.$$

For $\rho > 1/2$, it is this term that causes the mode to be localized along the edge at $n = 0$. The function $\bar{\alpha}(\omega)$ is a positive function we call the *envelope*, and the term $||\bar{\alpha}||_2$ is its total energy found by the integral

$$||\bar{\alpha}||_2 = \left(\int_{-\pi}^{\pi} d\omega\ \bar{\alpha}^2(\omega+\varphi_-)\right)^{1/2}.$$

Typical examples, using $\bar{\alpha}(\omega) = e^{-\omega^2}$, of such modes are seen in Figure 3. Integrating against the envelope in (7) modulates the monochromatic edge mode $\mathbf{a}_n^{Nu}(\omega)$ and generates the wave packet, or an edge mode that decays in both spatial directions on the lattice. The parameter ν controls the width of the wave packet. We can see this, for example, by choosing $\bar{\alpha}(\omega) = e^{-\omega^2}$, and then plotting $|\mathbf{A}^{(env)}_{m0}|$ for various values of ν; see Figure 4. As can be seen, as ν decreases, the width of the beam increases, thus leading to the notion of a *slowly-modulated-wave packet*. This broadening due to decreasing ν is a consequence of choosing $\mathbf{A}^{(env)}$ so that $\left|\left|\mathbf{A}^{(env)}\right|\right|_2 = 1$ for any $\nu > 0$. The envelope $\bar{\alpha}$ allows us to study effects arising from the localization of the edge mode in both spatial directions; *i.e.* we study two dimensionally localized modes. Note, equivalent expressions to those above can be found for zig-zag edges.

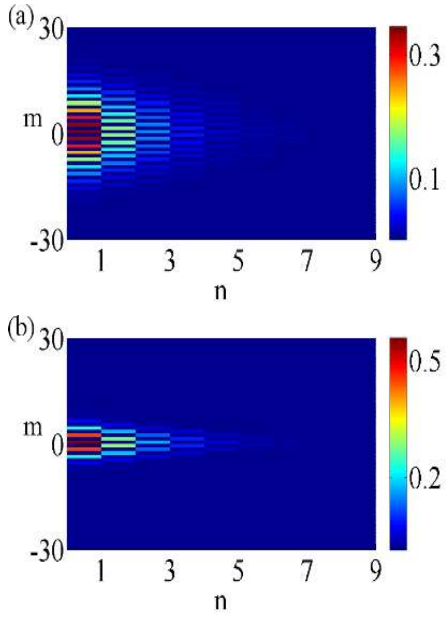

FIG. 3. (Color online) Typical stationary bearded edge modes. In (a), we have plotted (7) for $\nu = .2$, and in (b), we have plotted (7) for $\nu = .5$. In both figures, $\rho = 1$ and $\theta_1 = \theta_2 = \pi/4$.

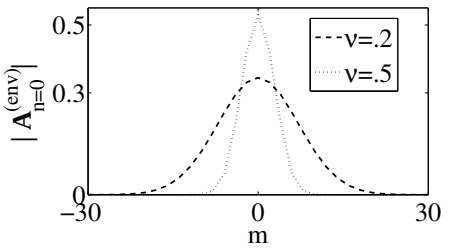

FIG. 4. Comparison of envelopes along bearded edge ($n = 0$). Smaller values of ν correspond to wider modes. In this figure, $\rho = 1$ and $\theta_1 = \theta_2 = \pi/4$.

D. Synopsis of Results

The details of how we generate the wave packet edge modes are presented in Section II. This is done for both edge geometries. We also explain the impact of deformation of the lattice ($\rho \neq 1$) on the different edge geometries. It is shown that the Dirac points in the continuous problem (1) manifest themselves as Dirac points in the dispersion bands of the discrete problem. Under deformation, we further show how the Dirac points merge and annihilate each other, which leads to the nonexistence of localized edge modes in the bearded edge geometry. Localized modes are supported in the zig-zag geometry even after the Dirac points have annihilated each other.

In Section IV, we find solutions to the weakly nonlinear problem of the form

$$\begin{pmatrix} \mathbf{A}(z) \\ \mathbf{B}(z) \end{pmatrix} \sim \begin{pmatrix} \exp\left(i\epsilon \left|\left|\mathbf{A}^{(env)}\right|\right|_4^4 z\right) \mathbf{A}^{(env)} \\ 0 \end{pmatrix} + \mathcal{O}(\min(\epsilon,\nu)) \tag{8}$$

for $z = \mathcal{O}(1/\max(\epsilon,\nu))$. As can be seen from the approximation, both the magnitude of the nonlinearity and the modulation of the wave packet are important in the underlying description. Note, while we have only stated this result for the bearded edge, an identical result can be shown for the zig-zag case, and so we only state the derivation of (8) for the bearded case for brevity. We thus get an $\mathcal{O}(\min(\epsilon,\nu))$ accurate approximation to the nonlinear evolution on a $\mathcal{O}(1/\max(\epsilon,\nu))$ timescale. We see that the nonlinearity introduces the slowly varying phase, or *self-phase modulation*,

$$\exp\left(i\epsilon \left|\left|\mathbf{A}^{(env)}\right|\right|_4^4 z\right), \tag{9}$$

as the leading order effect on the linear edge state. We likewise call (8) the *self-phase modulation approximation*. So while there is evolution in the phase, small to moderate nonlinearity does not cause the linear edge mode to scatter further into the bulk. But as shown in the numerical simulations for the bearded edge presented in Section III A, this nonlinearity does cause small, delocalized excitations along **B**-sites. There is excellent agreement between our asymptotic theory and numerical simulation.

The asymptotic approximation presented in Section IV is accurate only in the case of weak nonlinearity and sufficiently wide beams. However, in Section III B, we go beyond the case of weak nonlinearity and wide beams and present numerical simulations for cases of strong nonlinearity and relatively narrower beams. As shown, even strong nonlinearity does not significantly increase the amount of scattering into the bulk. Therefore, in all cases presented in this paper, we see localized zero-energy edge modes are robust to a variety of effects not previously studied.

II. ZERO-ENERGY LINEAR LOCALIZED MODES

Below we show how to find the zero-energy edge modes, *i.e.* ground states, or null solutions, for both edge geometries. The method to find wave packets is explained in detail in this section.

A. Bearded Edge

We assume the edge of the lattice is given by $\mathbf{A}_0$, and the only nearest neighbors the $\mathbf{A}_0$ sites see are the lattice sites in $\mathbf{B}_0$; see Figure 2(a). As shown in the Appendix, zero energy modes of the linear problem necessarily require that $\mathbf{B} = 0$, so that we are looking for solutions to

$\mathcal{L}_+\mathbf{A} = 0$. We then let

$$\mathbf{A}_{mn} = \mathbf{a}_n e^{im\omega},$$

so that the equation

$$\mathbf{A}_{mn} + \rho e^{i\theta_1}\mathbf{A}_{m+1,n+1} + \rho e^{i\theta_2}\mathbf{A}_{m-1,n+1} = 0,$$

becomes

$$\mathbf{a}_n(\omega) + \rho\gamma\mathbf{a}_{n+1}(\omega) = 0, \tag{10}$$

which has the solution

$$\mathbf{a}_n(\omega) = \left(-\frac{1}{\gamma(\omega)\rho}\right)^n \mathbf{a}_0(\omega),\ n \geq 0, \tag{11}$$

with

$$\gamma(\omega) = e^{i(\theta_1+\omega)} + e^{i(\theta_2-\omega)} = 2e^{i\varphi_+}\cos(\omega - \varphi_-), \tag{12}$$

where the definitions of $\varphi_\pm$ are given in (5).

Note, we see the role the edge plays since (10) would not have a decaying solution if n ran over all of the positive and negative integers. We get decay in (11) when $\rho|\gamma| > 1$, which is equivalent to

$$|\cos(\omega - \varphi_-)| > \frac{1}{2\rho}.$$

This inequality can only be satisfied if $\rho > 1/2$. Thus the bearded edge ceases to exist if $\rho \leq 1/2$. Further, we see that as $\rho|\gamma|$ gets closer to 1, or as ρ gets closer to $1/2$, the rate of decay, or degree of localization along the edge, of (11) decreases. In the case that $\rho > 1/2$, we see that $\omega \in \varphi_- + \mathcal{I}_{\tilde{\theta}}$ where

$$\mathcal{I}_{\tilde{\theta}} = [-\pi, -\pi + \tilde{\theta}) \cup (-\tilde{\theta}, \tilde{\theta}) \cup (\pi - \tilde{\theta}, \pi], \tag{13}$$

with

$$\tilde{\theta} = \cos^{-1}(1/2\rho).$$

Note, by $\omega \in \varphi_- + \mathcal{I}_{\tilde{\theta}}$ we mean those frequencies ω such that

$$\omega = \varphi_- + \tilde{\omega},\ \tilde{\omega} \in \mathcal{I}_{\tilde{\theta}}.$$

We then choose $\mathbf{a}_0(\omega) = \left(1 - \frac{1}{\rho^2|\gamma|^2}\right)^{1/2}$ and define

$$\mathbf{a}_n^{(Nu)}(\omega) = \left(1 - \frac{1}{\rho^2|\gamma|^2}\right)^{1/2}\left(-\frac{1}{\rho\gamma}\right)^n \tag{14}$$

so that we have that for $\omega \in \varphi_- + \mathcal{I}_{\tilde{\theta}}$,

$$\sum_{n=0}^{\infty}\left|\mathbf{a}_n^{(Nu)}(\omega)\right|^2 = 1.$$

To construct two dimensionally localized zero energy edge modes, we introduce an envelope $\alpha(\omega)$ and compute

$$\mathbf{A}_{mn}^{(Nu)} = \int_{\varphi_- + \mathcal{I}_{\tilde{\theta}}} d\omega\ \alpha(\omega)\mathbf{a}_n^{(Nu)}(\omega)e_m(\omega). \tag{15}$$

Note, we integrate strictly over the set $\varphi_- + \mathcal{I}_{\tilde{\theta}}$ since this represents the frequencies for which a zero-energy mode on a bearded edge exists.

In (6), if we look for non-stationary linear ($\epsilon = 0$) solutions of the form

$$\begin{pmatrix}\mathbf{A}(z)\\ \mathbf{B}(z)\end{pmatrix} = \begin{pmatrix}\mathbf{A}\\ \mathbf{B}\end{pmatrix}e^{-i\lambda z},$$

where we take λ to be real and non-zero, we get the problem

$$\begin{pmatrix}0 & \mathcal{L}_-\\ \mathcal{L}_+ & 0\end{pmatrix}\begin{pmatrix}\mathbf{A}\\ \mathbf{B}\end{pmatrix} = \lambda\begin{pmatrix}\mathbf{A}\\ \mathbf{B}\end{pmatrix}$$

Letting $\mathbf{A}$ and $\mathbf{B}$ be

$$\mathbf{A}_{mn} = \mathbf{a}_n e^{i\omega m},\ \mathbf{B}_{mn} = \mathbf{b}_n e^{i\omega m},$$

we get the reduced eigenvalue problem

$$\begin{pmatrix}0 & \mathcal{L}_{red}^-\\ \mathcal{L}_{red}^+ & 0\end{pmatrix}\begin{pmatrix}\mathbf{a}\\ \mathbf{b}\end{pmatrix} = \lambda\begin{pmatrix}\mathbf{a}\\ \mathbf{b}\end{pmatrix}.$$

where

$$\begin{aligned}(\mathcal{L}_{red}^-\mathbf{b})_n &= \rho\gamma^*\mathbf{b}_{n-1} + \mathbf{b}_n\\ (\mathcal{L}_{red}^+\mathbf{a})_n &= \rho\gamma\mathbf{a}_{n+1} + \mathbf{a}_n\end{aligned}$$

In order to compute the dispersion relation for $\lambda \neq 0$, it is convenient to reduce the two component system in $\mathbf{a}$ and $\mathbf{b}$ to a system in $\mathbf{b}$ alone supplemented with the boundary condition, due to the bearded edge, $\mathbf{b}_n = 0$ and $\mathbf{a}_n$ for $n < 0$. The reduced system becomes

$$\gamma^*\mathbf{b}_{n-1} + \gamma\mathbf{b}_{n+1} = \tilde{\lambda}\mathbf{b}_n. \tag{16}$$

with

$$\tilde{\lambda} = \left(\frac{\lambda^2 - 1}{\rho}\right) - \rho|\gamma|^2.$$

Using the boundary conditions on $\mathbf{b}_j$, we can solve the eigenvalue problem in $\tilde{\lambda}$. Letting $\mathbf{b}_n = r^n$ leads to the quadratic equation

$$r^2 - \frac{\tilde{\lambda}}{\gamma}r + \frac{\gamma^*}{\gamma} = 0,$$

which has the roots

$$r = \frac{1}{2\gamma}\left(\tilde{\lambda} \pm \sqrt{\tilde{\lambda}^2 - 4|\gamma|^2}\right).$$

In order to satisfy the initial condition $\mathbf{b}_1 = \tilde{\lambda}\mathbf{b}_0/\gamma$, we then get the solution

$$\mathbf{b}_n = \mathbf{b}_0\left(r_2^n + r_1\frac{r_1^n - r_2^n}{r_1 - r_2}\right) = \mathbf{b}_0 v_n,$$

where r_1 denotes the "+" branch, and r_2 denotes the "−" branch.

Since $|\gamma^*/\gamma| = 1$, then $|r_1 r_2| = 1$. To get bounded solutions for b_n, we then must have $|r_1| = |r_2| = 1$, since otherwise we must necessarily have that one of the r_j terms has magnitude larger than one while the other has magnitude smaller than one. In this case then, $\mathbf{b}_n$ would become unbounded as $n \to \infty$. We point out that for $|r_1| = |r_2| = 1$, $\mathbf{b}_n$ does not decay as $n \to \infty$, and thus for non-zero-energy modes, we do not get localization.

The restriction that $|r_j| = 1$ then gives the equations

$$2|\gamma| = \left|\tilde{\lambda} \pm \sqrt{\tilde{\lambda}^2 - 4|\gamma|^2}\right|$$

Since $\tilde{\lambda}$ must be real, we have two cases to study: $|\tilde{\lambda}| \leq 2|\gamma|$ and $|\tilde{\lambda}| > 2|\gamma|$. In the first case we see that

$$\left|\tilde{\lambda} \pm \sqrt{\tilde{\lambda}^2 - 4|\gamma|^2}\right| = \left|\tilde{\lambda} \pm i\sqrt{4|\gamma|^2 - \tilde{\lambda}^2}\right| = 2|\gamma|.$$

In the second case we must necessarily have that one of the roots r_j has magnitude larger than one, and thus the second case is not possible given the restriction on the size of the roots.

Therefore we only have $|r_j| = 1$ when $|\tilde{\lambda}| \leq 2|\gamma|$ and, the dispersion curve is found via the inequalities

$$|1 - \rho\,|\gamma(\omega)|\,| \leq |\lambda(\omega)| \leq 1 + \rho|\gamma(\omega)|. \tag{17}$$

For example, choosing $\theta_1 = \theta_2$ gives $\varphi_- = 0$ so that $|\gamma(\omega)| = 2|\cos(\omega)|$. We then get the dispersion bands as shown in Figure 5, where the shaded gray regions come from the inequality in (17).

For $\omega \sim \tilde{\theta}$, we see that

$$|1 - \rho|\gamma(\omega)|| \sim 2\rho|\sin(\tilde{\theta})||\omega - \tilde{\theta}|,$$

so that at $\tilde{\theta}$, the dispersion curves touch in a conical fashion, or meet at what we call, via analogy with Bloch bands, Dirac points. Similar calculations show that we have Dirac points, for $\rho > 1/2$, at the remaining edges of $\mathcal{I}_{\tilde{\theta}}$, *i.e.* $-\tilde{\theta}$, $-\pi + \tilde{\theta}$, and $\pi - \tilde{\theta}$. See Figure 5(a) for reference. Likewise, as shown in Figure 5(b), we see for $\rho < 1/2$ that the Dirac points have collided and vanished, thus prohibiting the existence of edge modes for the bearded case.

The edges of $\mathcal{I}_{\tilde{\theta}}$ are determined by the value $\tilde{\theta} = \cos^{-1}(1/2\rho)$, which as seen in [25], is the value used to distinguish the location of Dirac points in the Brillouin zone in the continuous model (1). Thus, we see that the Dirac points of the continuous problem determine the Dirac points of the discrete system. These results agree with those found in [17]. However, we point out that neither numerical simulations or other approximations were used to generate these results.

B. Zig-Zag Edge

By a zig-zag edge, we mean an edge ending in only **B** lattice sites; see Figure 2(b). For zero-energy localized modes to exist, as explained in the Appendix, we necessarily have that $\mathbf{A} = 0$, so that we must solve $\mathcal{L}_-\mathbf{B} = 0$. In this case, we can repeat the analysis we used in the bearded case to get that a **B** site zero energy solution exists when $\rho|\gamma(\omega)| < 1$, or

$$|\cos(\omega - \varphi_-)| < \frac{1}{2\rho},$$

which holds for some ω for $\rho \geq 0$.

This zero energy solution, say $\mathbf{B}^{(Nu)}$, is given by

$$\mathbf{B}^{(Nu)}_{mn} = \int_{\varphi_- + \mathcal{I}^c_{\tilde{\theta}}} d\omega \beta(\omega) \mathbf{b}^{(Nu)}_n(\omega) e_m(\omega),$$

where,

$$\mathcal{I}^c_{\tilde{\theta}} = (-\pi + \tilde{\theta}, -\tilde{\theta}) \cup (\tilde{\theta}, \pi - \tilde{\theta}), \tag{18}$$

and where, denoting the conjugate of γ, see (12), by γ^*,

$$\mathbf{b}^{(Nu)}_n(\omega) = \left(1 - \rho^2|\gamma(\omega)|^2\right)^{1/2} \left(-\rho\gamma^*(\omega)\right)^n.$$

As indicated earlier, the frequency condition for the existence of the bearded zero energy solutions, *i.e.* $\rho|\gamma| > 1$, and the zig-zag zero energy solutions, *i.e.* $\rho|\gamma| < 1$, exist on complimentary sets; compare (13) to (18). Further, we can repeat the analysis from above and show that the dispersion curves are again given by (17); see Figure 6. We note that the zig-zag edge zero energy states exist at frequencies complementary to those at which one finds bearded edge states; this is indicated by the horizontal line in Figure 6(a).

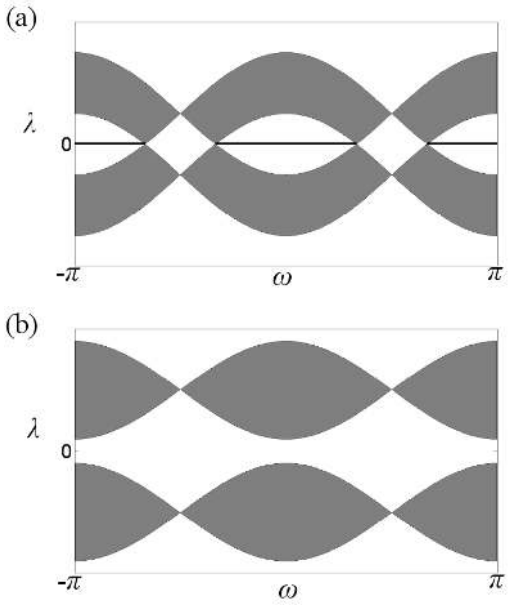

FIG. 5. The shaded areas represent (17); the horizontal lines represent zero energy modes. In (a), for $\rho = 1 > 1/2$, the zero energy bearded edge modes exist at frequencies in $\mathcal{I}_{\tilde{\theta}}$; they touch the Dirac points at $\pm\tilde{\theta}$, $-\pi + \tilde{\theta}$, and $\pi - \tilde{\theta}$. In (b), we see that for $\rho = .4 < 1/2$, the zero energy bearded edge states no longer exist and the bands have completely separated. In both figures we have chosen $\varphi_- = 0$.

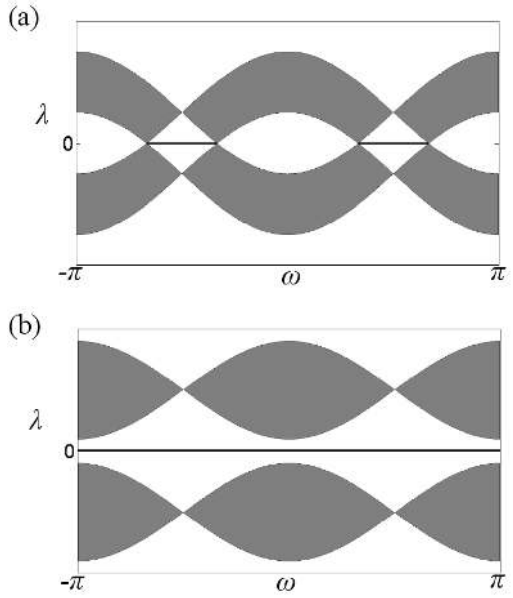

FIG. 6. The shaded areas represent (17); the horizontal lines represent zero energy modes. In (a), for $\rho = 1 > 1/2$, the zero energy zig-zag edge modes exist at frequencies in $\mathcal{I}_{\tilde{\theta}}^{c}$. In (b), we see that for $\rho = .4 < 1/2$, the zig-zag edge zero energy modes exist for all possible frequencies. In both figures we have chosen $\varphi_- = 0$.

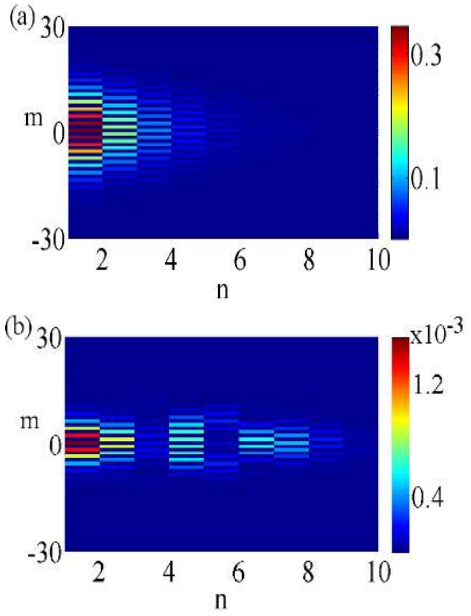

FIG. 7. (Color online) Edge modes at $z = 5$ for $\rho = 1, \theta_1 = \theta_2 = \pi/4$ on the **A**-sites in (a) and the **B**-sites in (b). We take weak nonlinearity ($\epsilon = .2$) and a wide beam ($\nu = .2$). Localization along the edge is maintained up to $z = 5 = 1/\epsilon$. The size of the induced B component is small.

III. NUMERICAL SIMULATIONS OF THE IMPACT OF NONLINEARITY

Throughout this section, we look only at the case of the impact of nonlinearity on modes supported on bearded edges. In the simulations of (6) we apply the following initial condition at $z = 0$

$$\begin{pmatrix} \mathbf{A}(0) \\ \mathbf{B}(0) \end{pmatrix} = \begin{pmatrix} \mathbf{A}^{(env)} \\ 0 \end{pmatrix}.$$

where $\mathbf{A}^{(env)}$ is defined in (7). See Figure 3 for a plot of typical initial conditions. We now study via numerical simulation how the evolution of zero-energy linear edge modes are affected by nonlinearity and variation in the width of the mode. When computing $\mathbf{A}^{(env)}$, we take $\bar{\alpha}(\omega) = e^{-\omega^2}$.

A. Edge States with Weak Nonlinearities and Confirmation of Self-Phase Modulation Approximation

For weak nonlinearity ($\epsilon = .2$), and a wide beam ($\nu = .2$), we plot in Figure 7 the result of propagating the fields on the **A** and **B** sites for a distance $z = 1/\epsilon = 5$. As shown in Figure 7(b), setting the magnitude of the nonlinearity to be $\mathcal{O}(\epsilon)$ causes weak delocalization along the edge. This agrees with the asymptotic approximation (8) (valid for length scales up to $z = \mathcal{O}(1/\epsilon)$) that the first order correction due to nonlinearity is weak self-phase modulation, which does not affect the localization of the leading order solution.

In Figure 8, we plot the error which is the maximum difference between the numerically computed solution and the asymptotic solution (8), *i.e.* we compute

$$\max_{m,n} \left\{ \left| \mathbf{A}_{mn}^{num}(z) - \mathbf{A}_{mn}^{asym}(z) \right|, \left| \mathbf{B}_{mn}^{num}(z) - \mathbf{B}_{mn}^{asym}(z) \right| \right\}.$$

We see that the difference between our asymptotic approximation and the numerical simulation is small, and by halving ϵ and ν, we reduce the error more than half after propagating twice as far. In Figure 9, we compare the phase of the maximum amplitude part of the numerical solution to the phase computed from (9). The self-phase modulation approximation predicts a linear evolution of the phase in response to weak nonlinearity and this agrees with the numerical solution. Further, our approximation correctly shows the order of the phase in the presence of weak nonlinearity is $\mathcal{O}(\nu)$, see (22). This can be deduced by comparing Figure 9(a) to 9(b), in which reducing ν from 0.2 to 0.1 reduces the phase at any z by half.

Therefore, we have numerical agreement with our theoretical prediction (8) that weak nonlinearity has only a small delocalizing effect on a sufficiently wide linear edge state. We also point out that by looking at wave-packets, we see spatial effects, in particular in Figure 7(b). We note, as seen in Figure 10 that localization also holds even if we take $z \sim \mathcal{O}(1/\epsilon\nu) = 25$, in which case the slow self-phase modulation and weak nonlinearity both have an asymptotically long time to act.

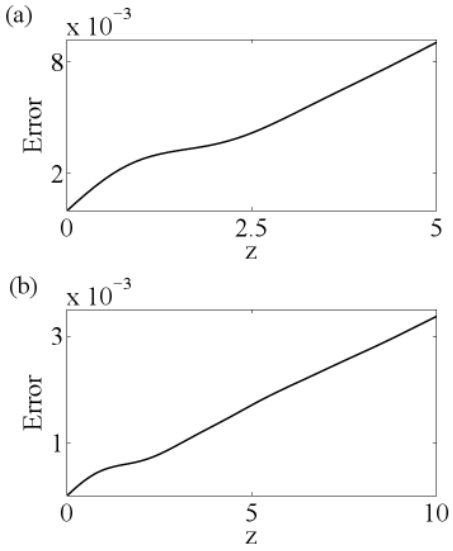

FIG. 8. ($\rho = 1, \theta_1 = \theta_2 = \pi/4$) Comparing (a), the error between the asymptotics and numerics for $\epsilon = \nu = .2$, and (b), which gives the error for $\epsilon = \nu = .1$, by halving ϵ and ν, the error is reduced by half even though we propagate twice as far in (b).

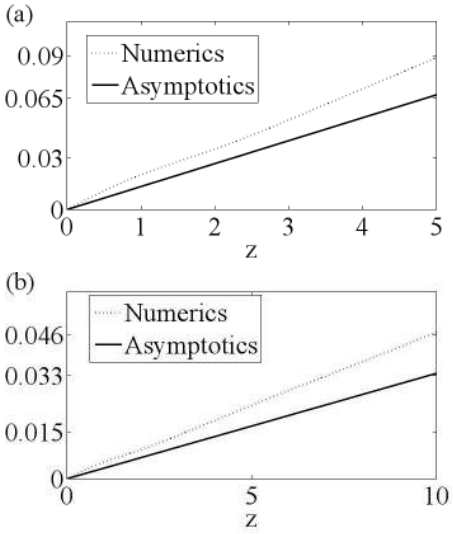

FIG. 9. ($\rho = 1, \theta_1 = \theta_2 = \pi/4$) In (a), we have plotted the analytically and numerically computed phases for $\epsilon = \nu = .2$; in (b), we plot the case $\epsilon = \nu = .1$. By comparing (a) and (b), by halving ϵ and ν, the numerically computed phase is reduced by half even though we propagate twice as far in (b).

It is also interesting to look at the case of $\rho = .55$ which is close to the critical value at which edge modes in the bearded edge cease to exist. As shown in Figure 11, the modes, as expected, are less localized since the rate of decay of the linear edge mode is significantly slower in the case of $\rho = .55$ than the case of $\rho = 1$; see (11) and associated discussion. However, we see from Figure 12, that the slow self-phase modulation approximation (8) is still an excellent approximation to the dynamics. Thus, while the edge mode for $\rho = .55$ is less localized, the nonlinearity does not introduce any further delocalization. Likewise, we see that (8) is still valid in the bearded edge case even as ρ gets close to the critical value of $1/2$.

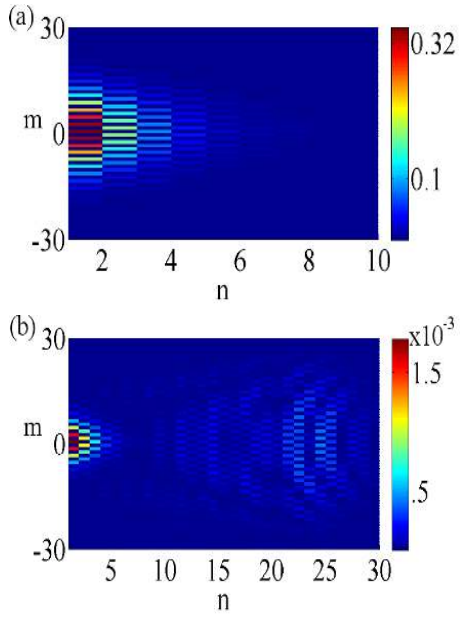

FIG. 10. (Color online) Edge modes at $z = 25$ for $\rho = 1, \theta_1 = \theta_2 = \pi/4$, and weak nonlinearity ($\epsilon = .2$) and wide beam ($\nu = .2$) on the **A**-sites in (a) and the **B**-sites in (b). Localization along the edge is maintained up to $z = 25 = 1/(\nu\epsilon)$. The size of the induced B component is small.

B. Edge States with Strong Nonlinearities

Going beyond our asymptotic theory, we present numerical results for the case of strong nonlinearity, $\epsilon = 1$, and a relatively narrower beam, $\nu = 0.5$ (*cf.* Figure 4). The narrower beam can also be described as a rapid modulation. The combined impact of these effects leads to greater delocalization, as can be seen in Figure 13(b). However, as indicated in 14(b), which is a plot of the quantity $(\sum_{m,n} |\mathbf{B}_{mn}(z)|^2)^{1/2}$, given that we begin with total energy equal to one between both **A** and **B** sites, then Figure 14(b) shows for $z \sim 10 = 5/(\epsilon\nu)$ that about 13 % of the total energy has been transferred into the **B** mode. We further see from Figures 13(a) and 14(a), that most of the energy, more than 82 %, as measured by the quantity $(\sum_m |\mathbf{A}_{m0}(z)|^2)^{1/2}$ remains localized along the **A** edge sites. This leaves approximately 5 % of the energy in the bulk **A** sites. Therefore we see that localized linear edge modes essentially persist in the presence of large nonlinearities.

It is also interesting to consider the case $\rho \sim 1/2$; we choose $\rho = 0.55$. As before, we take $\epsilon = 1$ and $\nu = 0.5$, so that we are still looking at the case of strong

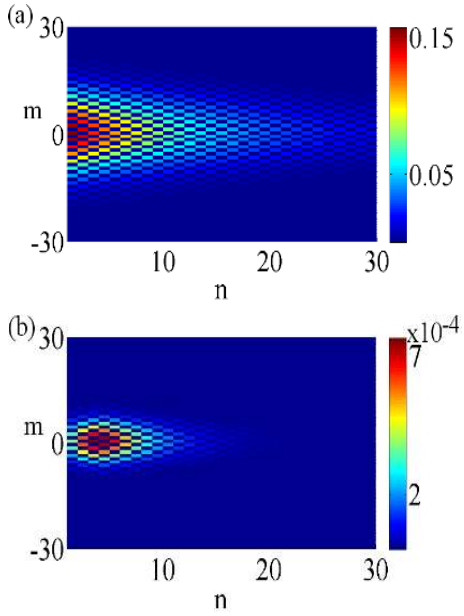

FIG. 11. (Color online) Edge modes at $z = 5$ for $\rho = .55, \theta_1 = \theta_2 = \pi/4$, and weak nonlinearity ($\epsilon = .2$) and wide beam ($\nu = .2$) on the **A**-sites in (a) and the **B**-sites in (b). The nonlinearity does not introduce any significant further delocalization of the edge mode.

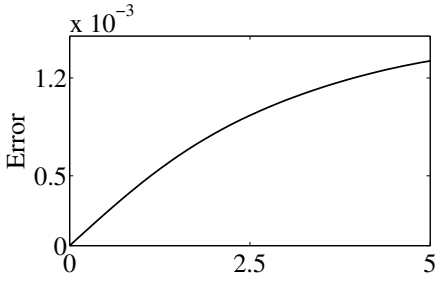

FIG. 12. ($\theta_1 = \theta_2 = \pi/4$) Maximum error between asymptotics and numerics for $\epsilon = \nu = .2$ and $\rho = .55$.

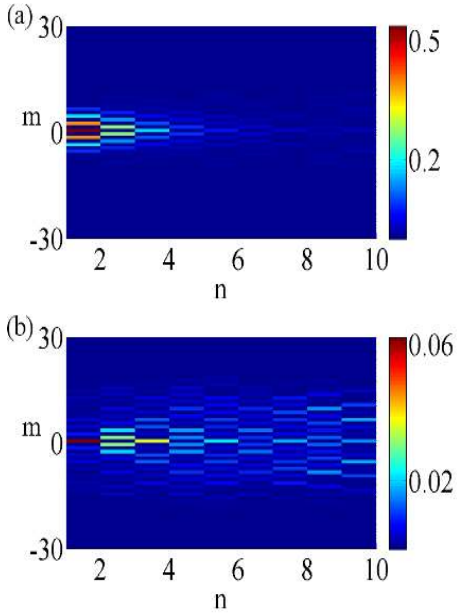

FIG. 13. (Color online) Edge modes at $z = 10$ for $\rho = 1, \theta_1 = \theta_2 = \pi/4$, and strong nonlinearity ($\epsilon = 1$) and narrow beam ($\nu = .5$) on the **A**-sites in (a) and the **B**-sites in (b). Localization along the edge is maintained up to $z = 10$.

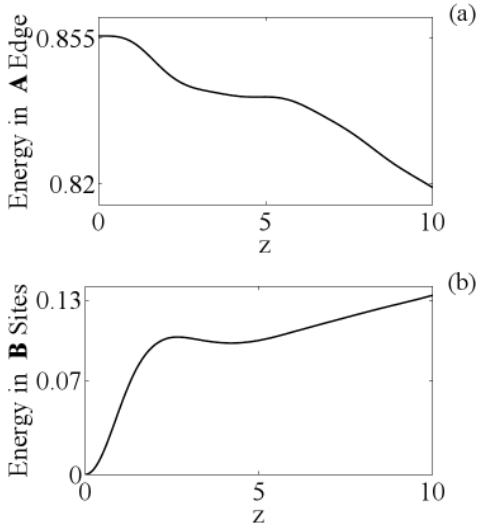

FIG. 14. ($\rho = 1, \theta_1 = \theta_2 = \pi/4$). For large nonlinearity ($\epsilon = 1$) and narrow beam ($\nu = .5$), in (a) we plot $(\sum_m |\mathbf{A}_{m0}(z)|^2)^{1/2}$, or the energy on the **A** edge. In (b) we plot the total energy, $(\sum_{m,n} |\mathbf{B}_{mn}(z)|^2)^{1/2}$, in all **B**-sites. The majority ($\sim 82\%$) of the energy is localized along **A**-edge sites as shown in (a). Some energy is leaked into the bulk along the **B**-sites as seen in (b).

nonlinearity and a relatively narrow beam. As can be seen from Figure 15(a), the degree of localization for $\rho \sim 1/2$ is less than for $\rho = 1$. However, as was the case for weak nonlinearity and slow modulation, *i.e.* $\epsilon = \nu = .2$ with $\rho = 0.55$, the strong nonlinearity and relatively narrow beam width do not cause any significant amount of further scattering into the bulk. This can be seen from Figure 16(a), in which the amount of energy on the $n = 0$ edge changes very little as the beam propagates through the lattice. Likewise, we see from Figure 16(b) that only a small amount of energy, $\sim 5\%$, is scattered into the **B** sites.

IV. DERIVATION OF THE SELF-PHASE MODULATION APPROXIMATION

In this section we show how to derive equation (8). Hereafter, we will only explicitly mention the bearded

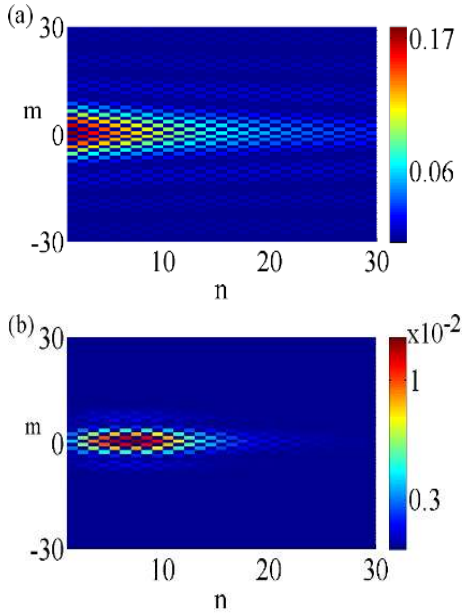

FIG. 15. (Color online) Edge modes at $z = 10$ for $\rho = .55, \theta_1 = \theta_2 = \pi/4$, and strong nonlinearity ($\epsilon = 1$) and narrow beam ($\nu = .5$) on the **A**-sites in (a) and the **B**-sites in (b). For $\rho \sim 1/2$, more energy is scattered into the bulk along both **A** and **B** sites.

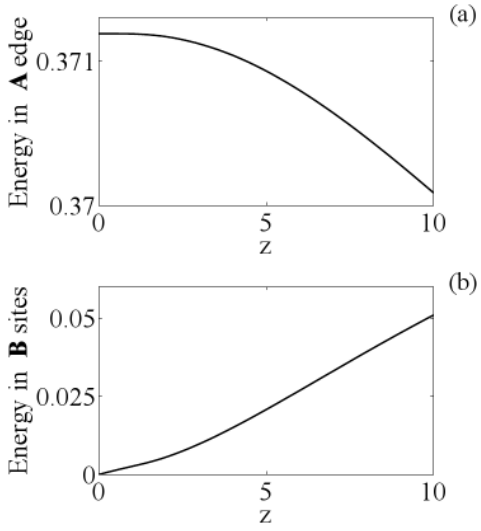

FIG. 16. ($\rho = .55, \theta_1 = \theta_2 = \pi/4$) For large nonlinearity ($\epsilon = 1$) and narrow beam ($\nu = .5$), in (a) we plot $(\sum_m |\mathbf{A}_{m0}(z)|^2)^{1/2}$, or the energy on the **A** edge. In (b) we plot the total energy, $(\sum_{m,n} |\mathbf{B}_{mn}(z)|^2)^{1/2}$, in all **B**-sites. From (a), we see less than 1% of the energy on the edge is scattered into the bulk. As seen in (b), energy scatters into **B** sites in a steadier way, but the amount of energy scattered into the **B** sites is still small.

case, and assume $\rho > 1/2$. The choice of a bearded edge does not play a critical role, and a self-phase modulation approximation could be found for the zig-zag case following similar arguments.

We assume the following ansatz for the solution to (6)

$$\begin{pmatrix} \mathbf{A}(z) \\ \mathbf{B}(z) \end{pmatrix} = c(\epsilon z) \begin{pmatrix} \mathbf{A}^{(Nu)} \\ 0 \end{pmatrix} + \epsilon \vec{\mathbf{R}}(z),$$

where

$$\vec{\mathbf{R}}(z) = \begin{pmatrix} \mathbf{R}_1(z) \\ \mathbf{R}_2(z) \end{pmatrix},$$

and we define the slow spatial scale $\tilde{Z} = \epsilon z$. Substituting this ansatz into equation (6), we get the following equation for the remainder $\vec{\mathbf{R}}$

$$-i\partial_z \vec{\mathbf{R}} \sim \mathcal{L}\vec{\mathbf{R}} + \begin{pmatrix} \mathcal{N}(\mathbf{A}^{(Nu)}) \\ 0 \end{pmatrix},$$

where

$$\mathcal{L} = \begin{pmatrix} 0 & \mathcal{L}_- \\ \mathcal{L}_+ & 0 \end{pmatrix}.$$

Using variation of parameters we can write the leading order solution to this forced problem in the form

$$\vec{\mathbf{R}}(z) \sim i \int_0^z e^{i\mathcal{L}(z-s)} \begin{pmatrix} \mathcal{N}(\mathbf{A}^{(Nu)}) \\ 0 \end{pmatrix} ds$$

where

$$\mathcal{N}(\mathbf{A}^{(Nu)}) = i\mathbf{A}^{(Nu)}\partial_{\tilde{Z}} c + |\mathbf{A}^{(Nu)}|^2 \mathbf{A}^{(Nu)} |c|^2 c,$$

with $\vec{\mathbf{R}}(0) = 0$. We note that if $\mathcal{L}\vec{\mathbf{F}} = 0$ then $e^{-i\mathcal{L}s}\vec{\mathbf{F}} = \vec{\mathbf{F}}$ since

$$e^{-i\mathcal{L}s}\vec{\mathbf{F}} = \left(I - is\mathcal{L} - \frac{s^2}{2!}\mathcal{L}^2 + \cdots \right) F = F,$$

so that

$$\int_0^z e^{i\mathcal{L}(z-s)} \vec{\mathbf{F}} ds = z\vec{\mathbf{F}},$$

or zero energy solutions of $\mathcal{L}$ give rise to secularities.

Thus, in order to remove all terms which have growth in z, noting for the bearded edge that any zero energy solution is of the form

$$\begin{pmatrix} \mathbf{A} \\ 0 \end{pmatrix}, \ \mathcal{L}_+ \mathbf{A} = 0,$$

we then want

$$P_{Nu,+} \mathcal{N}(\mathbf{A}^{(Nu)}) = 0.$$

where $P_{Nu,+}$ denotes the projection onto the null space of $\mathcal{L}_+$. We thus need to find the null space of $\mathcal{L}_+$, say $\ker(\mathcal{L}_+)$.

To find $\ker(\mathcal{L}_+)$, we write the envelope $\alpha(\omega)$ in (15) as a Fourier series

$$\alpha(\omega) = \sum_{l=-\infty}^{\infty} \hat{\alpha}_l e_l(\omega),$$

so that we have

$$\mathbf{A}^{(Nu)}_{mn} = \sum_{l=-\infty}^{\infty} \hat{\alpha}_l \left(\mathbf{K}_l\right)_{mn},$$

where

$$\begin{aligned}\left(\mathbf{K}_l\right)_{mn} =& \int_{-\pi+\varphi_-}^{\pi+\varphi_-} d\omega\ \mathbf{a}^{(Nu)}_n(\omega) e_l(\omega) e_m(\omega) \\ =& \int_{\varphi_-+\mathcal{I}_{\tilde{\theta}}} d\omega\ \mathbf{a}^{(Nu)}_n(\omega) e_l(\omega) e_m(\omega).\end{aligned}$$

Note, the last equality comes from (14) which required for a bearded edge that $\mathbf{a}^{(Nu)}_n(\omega) = 0$ if $\omega \notin \varphi_- + \mathcal{I}_{\tilde{\theta}}$. One can show that the set $\{\mathbf{K}_l\}_{l=-\infty}^{\infty}$ is an orthonormal basis of $\ker(\mathcal{L}_+)$.

Therefore, the condition $P_{Nu,+}\mathbf{A}^{(nl)} = 0$ is equivalent to the condition

$$\left|\left|P_{Nu,+}\mathcal{N}(\mathbf{A}^{(Nu)})\right|\right|_2^2 = \sum_{l=-\infty}^{\infty} \left|\left\langle \mathcal{N}(\mathbf{A}^{(Nu)}), \mathbf{K}_l \right\rangle\right|^2 = 0.$$

Letting $c(\tilde{Z}) = e^{i\Omega\tilde{Z}}$, we see that

$$\begin{aligned}\left|\left\langle \mathcal{N}(\mathbf{A}^{(Nu)}), \mathbf{K}_l \right\rangle\right|^2 =& \left|\left\langle -\Omega\mathbf{A}^{(Nu)} + |\mathbf{A}^{(Nu)}|^2\mathbf{A}^{(Nu)}, \mathbf{K}_l \right\rangle\right|^2 \\ =& \Omega^2 \left|\left\langle \mathbf{A}^{(Nu)}, \mathbf{K}_l \right\rangle\right|^2 \\ & - 2\Omega \left\langle |\mathbf{A}^{(Nu)}|^2\mathbf{A}^{(Nu)}, \mathbf{K}_l \right\rangle \left\langle \mathbf{K}_l, \mathbf{A}^{(Nu)} \right\rangle \\ & + \left|\left\langle |\mathbf{A}^{(Nu)}|^2\mathbf{A}^{(Nu)}, \mathbf{K}_l \right\rangle\right|^2.\end{aligned}$$

Summing over the index l then gives

$$\begin{aligned}\left|\left|P_{Nu,+}\mathcal{N}(\mathbf{A}^{(Nu)})\right|\right|_2^2 =& \Omega^2 \left|\left|\mathbf{A}^{(Nu)}\right|\right|_2^2 - 2\Omega \left|\left|\mathbf{A}^{(Nu)}\right|\right|_4^4 \\ & + \left|\left|P_{Nu,+}|\mathbf{A}^{(Nu)}|^2\mathbf{A}^{(Nu)}\right|\right|_2^2,\end{aligned}$$

where we have used the fact that

$$\begin{aligned}\left|\left|\mathbf{A}^{(Nu)}\right|\right|_4^4 =& \left\langle |\mathbf{A}^{(Nu)}|^2\mathbf{A}^{(Nu)}, \mathbf{A}^{(Nu)} \right\rangle \\ =& \sum_{l=-\infty}^{\infty} \left\langle |\mathbf{A}^{(Nu)}|^2\mathbf{A}^{(Nu)}, \mathbf{K}_l \right\rangle \left\langle \mathbf{K}_l, \mathbf{A}^{(Nu)} \right\rangle,\end{aligned}$$

since $\mathbf{A}^{(Nu)} \in \ker(\mathcal{L}_+)$.

Since $\left|\left|P_{Nu,+}\mathbf{A}^{(nl)}\right|\right|_2^2 \geq 0$, the best we can hope to do is minimize this quantity which leads to choosing Ω to be

$$\Omega = \Omega(\mathbf{A}^{(Nu)}) = \frac{\left|\left|\mathbf{A}^{(Nu)}\right|\right|_4^4}{\left|\left|\mathbf{A}^{(Nu)}\right|\right|_2^2}. \tag{19}$$

Likewise, we see that by choosing Ω as we have, we get the minimal value of $\left|\left|P_{Nu,+}\mathbf{A}^{(nl)}\right|\right|_2$, which we call $S(\mathbf{A}^{(Nu)})$, to be

$$S^2(\mathbf{A}^{(Nu)}) = \left|\left|P_{Nu,+}|\mathbf{A}^{(Nu)}|^2\mathbf{A}^{(Nu)}\right|\right|_2^2 - \frac{\left|\left|\mathbf{A}^{(Nu)}\right|\right|_4^8}{\left|\left|\mathbf{A}^{(Nu)}\right|\right|_2^2}.$$

This gives us the leading order solution

$$\begin{pmatrix}\mathbf{A}(z)\\ \mathbf{B}(z)\end{pmatrix} = e^{i\epsilon\Omega(\mathbf{A}^{(Nu)})z}\begin{pmatrix}\mathbf{A}^{(Nu)}\\ 0\end{pmatrix} + \mathcal{O}(\epsilon S(\mathbf{A}^{(Nu)})z). \tag{20}$$

In order to get a valid asymptotic approximation, we need to make $S(\mathbf{A}^{(Nu)})$ as small as possible.

A means to controlling $S(\mathbf{A}^{(Nu)})$ is to choose a positive function $\bar{\alpha}(\nu)$ such that $\bar{\alpha}(\nu)$

$$\int_{-\infty}^{\infty} d\omega \bar{\alpha}(\omega) = 1.$$

We then choose the envelope that defines $\mathbf{A}^{(Nu)}$ to be

$$\alpha(\omega) = \frac{1}{\nu}\bar{\alpha}\left(\frac{\omega-\omega_0}{\nu}\right),$$

where $\omega_0 - \varphi_- \in \mathcal{I}_{\tilde{\theta}}$. While an arbitrary parameter, we choose $\omega_0 = 0$ for the sake of presentation. Thus in the case that $0 < \nu \ll 1$, we get that

$$\begin{aligned}\mathbf{A}^{(Nu)}_{mn} =& \frac{1}{\nu}\int_{-\pi+\varphi_-}^{\pi+\varphi_-} d\omega \bar{\alpha}\left(\frac{\omega}{\nu}\right) \mathbf{a}^{(Nu)}_n(\omega) e_m(\omega) \\ =& \int_{(-\pi+\varphi_-)/\nu}^{(\pi+\varphi_-)/\nu} d\omega \bar{\alpha}\left(\omega\right) \mathbf{a}^{(Nu)}_n(\nu\omega) e_m(\nu\omega) \\ =& \tilde{\alpha}(\nu m)\mathbf{a}^{(Nu)}_n(0) e_m(0) + \mathcal{O}(\nu),\end{aligned} \tag{21}$$

where

$$\tilde{\alpha}(\nu m) = \int_{-\infty}^{\infty} d\omega \bar{\alpha}\left(\omega\right) e_m(\nu\omega).$$

Thus, for small ν, we modulate the one-dimensional linear solution with a slowly varying envelope. We see that

$$\begin{aligned}\left|\left|\mathbf{A}^{(Nu)}\right|\right|_2^2 =& \int_{-\pi+\varphi_-}^{\pi+\varphi_-} d\omega \alpha^2(\omega+\varphi_-), \\ =& \frac{1}{\nu}\int_{(-\pi+\varphi_-)/\nu}^{(\pi+\varphi_-)/\nu} d\omega \bar{\alpha}^2(\omega+\varphi_-), \\ \sim& \frac{1}{\nu}\int_{-\infty}^{\infty} d\omega \bar{\alpha}^2(\omega+\varphi_-),\end{aligned}$$

and therefore $\left|\left|\mathbf{A}^{(Nu)}\right|\right|_2 = \mathcal{O}(1/\sqrt{\nu})$. In the Appendix we show

$$\left|\left|\mathbf{A}^{(Nu)}\right|\right|_4^4 = \mathcal{O}(1/\nu),$$

so that

$$\frac{\left|\left|\mathbf{A}^{(Nu)}\right|\right|_4^8}{\left|\left|\mathbf{A}^{(Nu)}\right|\right|_2^2} = \mathcal{O}(1/\nu),\ \nu \to 0^+.$$

Given that $|\mathbf{A}^{(Nu)}_{mn}| \leq 1$, then we also have that

$$\begin{aligned}\left|\left|P_{Nu,+}|\mathbf{A}^{(Nu)}|^2\mathbf{A}^{(Nu)}\right|\right|_2^2 \leq& \left|\left||\mathbf{A}^{(Nu)}|^2\mathbf{A}^{(Nu)}\right|\right|_2^2 \\ \leq& \left|\left|\mathbf{A}^{(Nu)}\right|\right|_2^2 = \mathcal{O}(1/\nu).\end{aligned}$$

As just shown, slow modulation of the wave packet is not enough to control $S(\mathbf{A}^{(Nu)})$. Therefore, we rescale $\mathbf{A}^{(Nu)}$ in the following way

$$\mathbf{A}^{(env)} = \frac{1}{\left|\left|\mathbf{A}^{(Nu)}\right|\right|_2}\mathbf{A}^{(Nu)},$$

so that

$$\mathbf{A}^{(env)}_{mn} = \frac{1}{\sqrt{\nu}\left|\left|\bar{\alpha}\right|\right|_2}\int_{-\pi+\varphi_-}^{\pi+\varphi_-} d\omega\bar{\alpha}\left(\frac{\omega}{\nu}\right)\mathbf{a}^{(Nu)}_n(\omega)e_m(\omega).$$

We then see that

$$\frac{\left|\left|\mathbf{A}^{(env)}\right|\right|_4^8}{\left|\left|\mathbf{A}^{(env)}\right|\right|_2^2} = \left|\left|\mathbf{A}^{(env)}\right|\right|_4^8 = \mathcal{O}(\nu^2),$$

and

$$\left|\left|P_{Nu,+}|\mathbf{A}^{(env)}|^2\mathbf{A}^{(env)}\right|\right|_2^2 = \mathcal{O}(\nu^2),$$

which then shows that $S(\mathbf{A}^{(env)}) = \mathcal{O}(\nu)$. Therefore, we have that

$$\begin{pmatrix}\mathbf{A}(z)\\ \mathbf{B}(z)\end{pmatrix} \sim e^{i\epsilon\Omega(\mathbf{A}^{(env)})z}\begin{pmatrix}\mathbf{A}^{(env)}\\ 0\end{pmatrix} + \mathcal{O}(\epsilon S(\mathbf{A}^{(env)})z),$$

where, using (19), we get the self-phase modulation term (9), *i.e.*

$$\Omega(\mathbf{A}^{(env)}) = \frac{\left|\left|\mathbf{A}^{(env)}\right|\right|_4^4}{\left|\left|\mathbf{A}^{(env)}\right|\right|_2^2} = \left|\left|\mathbf{A}^{(env)}\right|\right|_4^4,$$

since $\left|\left|\mathbf{A}^{(env)}\right|\right|_2 = 1$ by construction. Since $S(\mathbf{A}^{(env)}) = \mathcal{O}(\nu)$, then for $z \leq 1/\max(\epsilon,\nu)$, the error in using the self-phase modulation approximation is $\mathcal{O}(\min(\epsilon,\nu))$. We likewise see that

$$\Omega(\mathbf{A}^{(env)}) = \frac{\left|\left|\mathbf{A}^{(Nu)}\right|\right|_4^4}{\left|\left|\mathbf{A}^{(Nu)}\right|\right|_2^4} = \mathcal{O}(\nu), \tag{22}$$

since $\left|\left|\mathbf{A}^{(Nu)}\right|\right|_4^4 = \mathcal{O}(1/\nu)$, and $\left|\left|\mathbf{A}^{(Nu)}\right|\right|_2 = \mathcal{O}(1/\sqrt{\nu})$.

V. CONCLUSION

In this paper we find and analyze fully two dimensional localized edge modes. We study the impact of nonlinearity and spatial modulation on the associated zero-energy edge states in honeycomb optical lattices. It is shown both analytically and numerically, neither effect causes significant delocalization via the scattering of the modes into the bulk of the lattice. We further deduce that the response of an edge mode to weak nonlinearity and slow modulation is self-phase modulation. Even with strong nonlinearity two dimensional localized modes are found to persist in wide parameter regimes.

VI. ACKNOWLEDGEMENTS

This research was partially supported by the U.S. Air Force Office of Scientific Research, under grant FA9550-12-1-0207, by the NSF under grants CHE 1125935, and by the NSFC under grant 11204155.

APPENDIX

A. Details about the Lattice

The numbering scheme of lattice sites is of course arbitrary, but we adopt the following conventions. Given the numbering of $\mathbf{A}$ and $\mathbf{B}$ sites, if we have the sites $B_{m-1,n-1}$ and $B_{m+1,n-1}$, we do not have the site $B_{m,n-1}$, or we set $B_{m,n-1} = 0$. Likewise, if we have the sites $A_{m+1,n+1}$ and $A_{m-1,n+1}$ then we do not have the site $A_{m,n+1}$. See Figure 1 for clarification. This induces a staggered numbering system where we define the infinite dimensional vectors

$$\mathbf{A} = \begin{pmatrix}\vdots\\ \mathbf{A}_2\\ \mathbf{A}_1\\ \mathbf{A}_0\\ \mathbf{A}_{-1}\\ \mathbf{A}_{-2}\\ \vdots\end{pmatrix},\ \mathbf{B} = \begin{pmatrix}\vdots\\ \mathbf{B}_2\\ \mathbf{B}_1\\ \mathbf{B}_0\\ \mathbf{B}_{-1}\\ \mathbf{B}_{-2}\\ \vdots\end{pmatrix},$$

where $\mathbf{A}_{2l}$ and $\mathbf{B}_{2l}$ are staggered in an even fashion, *i.e.*

$$\mathbf{A}_{2j} = \begin{pmatrix}\vdots\\ A_{2,2j}\\ 0\\ A_{0,2j}\\ 0\\ A_{-2,2j}\\ \vdots\end{pmatrix},\ \mathbf{B}_{2j} = \begin{pmatrix}\vdots\\ B_{2,2j}\\ 0\\ B_{0,2j}\\ 0\\ B_{-2,2j}\\ \vdots\end{pmatrix}.$$

The odd terms, $\mathbf{A}_{2l+1}$ and $\mathbf{B}_{2l+1}$, are staggered in an odd fashion.

1. Bearded Edge

In this case, we assume the edge of the lattice is given by $\mathbf{A}_0$ with even staggering, and the only nearest neighbors the $\mathbf{A}_0$ sites see are the lattice sites in $\mathbf{B}_0$. Thus we have $\mathbf{A}_k = \mathbf{B}_k = 0$ for $k < 0$. See Figure 2(a) for details. Since $\mathbf{A}_0$ only interacts with $\mathbf{B}_0$ we have

$$\mathcal{L}_- = \begin{pmatrix}\ddots & \ddots & \ddots & \ddots & \ddots & \vdots\\ \cdots & 0 & 0 & I & L_o & 0\\ \cdots & 0 & 0 & 0 & I & L_e\\ \cdots & 0 & 0 & 0 & 0 & I\end{pmatrix},$$

and

$$\mathcal{L}_+ = \begin{pmatrix} \ddots & \ddots & \ddots & \ddots & \ddots & \vdots \\ \cdots & 0 & L_e^\dagger & I & 0 & 0 \\ \cdots & 0 & 0 & L_o^\dagger & I & 0 \\ \cdots & 0 & 0 & 0 & L_e^\dagger & I \end{pmatrix},$$

where the † denotes the Hermitian conjugate of an operator. We then have

$$\mathcal{L}_-\mathbf{B} = \begin{pmatrix} \vdots \\ \mathbf{B}_2 + L_o\mathbf{B}_1 \\ \mathbf{B}_1 + L_e\mathbf{B}_0 \\ \mathbf{B}_0 \end{pmatrix}, \ \mathcal{L}_+\mathbf{A} = \begin{pmatrix} \vdots \\ \mathbf{A}_2 + L_e^\dagger\mathbf{A}_3 \\ \mathbf{A}_1 + L_o^\dagger\mathbf{A}_2 \\ \mathbf{A}_0 + L_e^\dagger\mathbf{A}_1 \end{pmatrix},$$

where for j odd we have

$$(L_o\mathbf{B}_j)_m = \begin{cases} 0, & m \text{ odd}, \\ \rho e^{-i\theta_2}B_{m+1,j} + \rho e^{-i\theta_1}B_{m-1,j}, & m \text{ even}, \end{cases}$$

$$\left(L_e^\dagger\mathbf{A}_j\right)_m = \begin{cases} 0, & m \text{ odd}, \\ \rho e^{i\theta_2}A_{m-1,j} + \rho e^{i\theta_1}A_{m+1,j}, & m \text{ even}, \end{cases}$$

and for j even we have

$$(L_e\mathbf{B}_j)_m = \begin{cases} 0, & m \text{ even}, \\ \rho e^{-i\theta_2}B_{m+1,j} + \rho e^{-i\theta_1}B_{m-1,j}, & m \text{ odd}, \end{cases}$$

$$\left(L_o^\dagger\mathbf{A}_j\right)_m = \begin{cases} 0, & m \text{ even}, \\ \rho e^{i\theta_2}A_{m-1,j} + \rho e^{i\theta_1}A_{m+1,j}, & m \text{ odd}. \end{cases}$$

From this, we now see why for the zero-energy states that $\mathbf{B}$ must be zero since from $\mathcal{L}_-\mathbf{B} = 0$ we have that $\mathbf{B}_0 = 0$, which would then give that $\mathbf{B}_1 = 0$, and so forth.

2. Zig-Zag Edge

Here, we are describing an edge ending in only $\mathbf{B}$ lattice sites which see only the two forward interactions of the three nearest neighbor interactions. In this case, we treat $\mathbf{B}_0$ as the edge sites with an even staggering, so that $\mathbf{B}_k = 0$ for $k < 0$. This forces us to set $\mathbf{A}_k = 0$ for $k \leq 0$. See Figure 2(b) for clarification. Thus, for the zig-zag edge, we have

$$\mathbf{A} = \begin{pmatrix} \vdots \\ \mathbf{A}_2 \\ \mathbf{A}_1 \\ 0 \end{pmatrix}, \ \mathbf{B} = \begin{pmatrix} \vdots \\ \mathbf{B}_2 \\ \mathbf{B}_1 \\ \mathbf{B}_0 \end{pmatrix}.$$

This choice requires slight modifications to $\mathcal{L}_-$ and $\mathcal{L}_+$. In particular, the identity matrices do not appear along the diagonal. Instead, we have that

$$\mathcal{L}_- = \begin{pmatrix} \ddots & \ddots & \ddots & \ddots & \ddots & \vdots \\ \cdots & 0 & 0 & I & L_o & 0 \\ \cdots & 0 & 0 & 0 & I & L_e \end{pmatrix},$$

and

$$\mathcal{L}_+ = \begin{pmatrix} \cdots & 0 & L_e^\dagger & I & 0 \\ \cdots & 0 & 0 & L_o^\dagger & I \\ \cdots & 0 & 0 & 0 & L_e^\dagger \end{pmatrix}.$$

Note, the infinite matrices are growing out from the bottom right corner, and $\mathcal{L}_-$ acts on the vector

$$\begin{pmatrix} \vdots \\ \mathbf{B}_2 \\ \mathbf{B}_1 \\ \mathbf{B}_0 \end{pmatrix},$$

while $\mathcal{L}_+$ acts on

$$\begin{pmatrix} \vdots \\ \mathbf{A}_2 \\ \mathbf{A}_1 \end{pmatrix}.$$

We note from $\mathcal{L}_+\mathbf{A} = 0$, we get the equation,

$$L_e^\dagger\mathbf{A}_1 = 0.$$

This gives us term by term the expression

$$\rho e^{i\theta_1}A_{1,m+1} + \rho e^{i\theta_2}A_{1,m-1} = 0,$$

or

$$A_{1,m+1} = e^{2i\varphi_{12}}A_{1,m-1}.$$

This gives $|A_{1,m+1}| = |A_{1,m-1}|$, and thus to get a decay solution as $m \to \infty$, we must take $\mathbf{A}_1 = 0$. This in turn gives $L_o^\dagger\mathbf{A}_2 = 0$, and so using the same argument we have $a_2 = 0$. Continuing in this way then shows that $\mathbf{A} = 0$.

B. Estimating $\left|\left|\mathbf{A}^{(Nu)}\right|\right|_4^4$

Using the envelope expansion (21), we get

$$\begin{aligned} \left|\left|\mathbf{A}^{(Nu)}\right|\right|_4^4 &\sim \left|\left|\mathbf{a}^{(Nu)}\right|\right|_4^4 \sum_{m=-\infty}^{\infty} |\bar{\alpha}(\nu m)|^4 \\ &\sim \left|\left|\mathbf{a}^{(Nu)}\right|\right|_4^4 \int_{\mathbb{R}^4} d^4\vec{\omega}\ \mathcal{A}(\vec{\omega})\mathcal{V}(\nu\vec{\omega}) \end{aligned}$$

where $\vec{\omega} = (\omega_1, \omega_2, \omega_3, \omega_4)$,

$$\mathcal{A}(\vec{\omega}) = \bar{\alpha}(\omega_1)\bar{\alpha}(\omega_2)\bar{\alpha}(\omega_3)\bar{\alpha}(\omega_4),$$

and

$$\mathcal{V}(\omega_1, \omega_2, \omega_3, \omega_4) = \sum_{m=-\infty}^{\infty} e_m(\omega_1)e_m(\omega_2)e_m^*(\omega_3)e_m^*(\omega_4).$$

Changing variables via $\tilde{\omega}_j = \nu\omega_j$, we then get

$$\left|\left|\mathbf{A}^{(Nu)}\right|\right|_4^4 \sim \frac{\left|\left|\mathbf{a}^{(Nu)}\right|\right|_4^4}{2\pi\nu^4} \int_{\mathbb{R}^3} d^3\vec{\tilde{\omega}}\mathcal{A}_s(\vec{\tilde{\omega}})\bar{\alpha}\left(\frac{\tilde{\omega}_1 + \tilde{\omega}_2 - \tilde{\omega}_3}{\nu}\right),$$

where

$$\mathcal{A}_s(\vec{\tilde{\omega}}) = \bar{\alpha}\left(\frac{\tilde{\omega}_1}{\nu}\right)\bar{\alpha}\left(\frac{\tilde{\omega}_2}{\nu}\right)\bar{\alpha}\left(\frac{\tilde{\omega}_3}{\nu}\right),$$

and where we have used

$$\sum_{m=-\infty}^{\infty} e_m(\tilde{\omega}_1)e_m(\tilde{\omega}_2)e_m^*(\tilde{\omega}_3)e_m^*(\tilde{\omega}_4) = \frac{1}{2\pi}\delta_{dr}(\tilde{\omega}_1+\tilde{\omega}_2-\tilde{\omega}_3-\tilde{\omega}_4),$$

with $\delta_{dr}(x)$ being the Dirac delta function. Returning then to the variables ω_j we have

$$\left|\left|\mathbf{A}^{(Nu)}\right|\right|_4^4 \sim \frac{\left|\left|\mathbf{a}^{(Nu)}\right|\right|_4^4}{2\pi\nu}\int_{\mathbb{R}^3} d^3\vec{\omega}\,\bar{\alpha}(\omega_1)\bar{\alpha}(\omega_2)\bar{\alpha}(\omega_3)\bar{\alpha}(\omega_1+\omega_2-\omega_3).$$

or

$$\left|\left|\mathbf{A}^{(Nu)}\right|\right|_4^4 = \mathcal{O}(1/\nu),\ \nu\to 0^+.$$

[1] J.W. Fleischer, T. Carmon, M. Segev, N.K. Efremidis, and D.N. Christodoulides. Observation of discrete solitons in optically induced real time waveguide arrays. *Phys. Rev. Lett.*, 90:023902, 2003.

[2] J. Yang, I. Makasyuk, A. Bezryadina, and Z. Chen. Dipole solitons in optically induced two-dimensional photonic lattices. *Opt. Lett.*, 29:1662, 2004.

[3] D.N. Neshev, T.J. Alexander, E.A. Ostrovskaya, Y.S. Kivshar, H. Martin, I. Makasyuk, and Z. Chen. Observation of discrete vortex solitons in optically induced photonic lattices. *Phys. Rev. Lett.*, 92:123903, 2004.

[4] X. Wang, Z. Chen, Y. Wang, and J. Yang. Observation of in-band lattice solitons. *Phys. Rev. Lett.*, 99:243901, 2007.

[5] M.J. Ablowitz, B. Ilan, E. Schonbrun, and R. Piestun. Solitons in two-dimensional lattices possessing defects, dislocations, and quasicrystal structures. *Phys. Rev. E*, 74:035601, 2006.

[6] L. Levi, M. Rechtsman, B. Freedman, T. Schwartz, O. Manela, and M. Segev. Dsiorder-enhanced transport in photonic quasicrystals. *Science*, 332:1541, 2011.

[7] M.J. Ablowitz, S. Nixon, and Y. Zhu. Conical diffraction in honeycomb lattices. *Phys. Rev. A*, 79:053830, 2009.

[8] O. Peleg, G. Bartal, B. Freedman, O. Menla, M. Segev, and D.N. Christodoulides. Conical diffraction and gap solitons in honeycomb photonic lattices. *Phys. Rev. Lett.*, 98:103901, 2007.

[9] P.G. Kevrekidis, B.A. Malomed, and Y.B. Gaididei. Solitons in triangular and honeycomb dynamical lattices with the cubic nonlinearity. *Phys. Rev. E*, 66:016609, 2002.

[10] M.C. Rechtsman, J. M. Zeuner, M. Heinrich, A. Tünnermann, M. Segev, and A. Szameit. Strain-induced pseudomagnetic field and Landau levels in photonic structures. *Nature Photonics*, 7:153–158, 2013.

[11] Z. Wang, Y. Chong, J.D. Joannopoulos, and M. Soljacic. Observation of unidirectional backscattering-immune topological electromagnetic states. *Nature*, 461:772–776, 2009.

[12] Y. Hatsugai. Edge states in the integer quantum Hall effect and the Riemann surface of the Bloch function. *Phys. Rev. B*, 48:851–862, 1993.

[13] M. Kohomoto and Y. Hasegawa. Zero modes and edge states of the honeycomb lattice. *Phys. Rev. B*, 76:205402, 2007.

[14] S. Ryu and Y. Hatsugai. Topological origin of zero-energy edge states in particle-hole symmetric systems. *Phys. Rev. Lett.*, 89:077002, 2002.

[15] D.J. Thouless, M. Kohmoto, M.P. Nightingale, and M. den Nijs. Quantitized Hall conductance in a two-dimensional periodic potential. *Phys. Rev. Lett.*, 49:405–408, 1982.

[16] Y. Plotnik, M.C. Rechtsman, D. Song, M. Heinrich, A. Szameit, N. Malkova, Z. Chen, and M. Segev. Observation of dispersion-free edge states in honeycomb photonic lattices. *Quantum Electronics and Laser Science Conference - Periodic Materials Phenomena*, 2012.

[17] M.C. Rechtsman, Y. Plotnik, J.M. Zeuner, A. Szameit, and M. Segev. Topological creation and destruction of edge states in photonic graphene. *arXiv:cond-mat.mes-hall*, 1211:5683v1, 2012.

[18] K. Fang, Z. Yu, and S. Fan. Microscopic theory of photonic one-way edge mode. *Phys. Rev. B*, 84:075477, 2011.

[19] F.D.M Haldane and S. Raghu. Possible realization of directional optical wavesguides in photonic crystals with broken time-reversal symmetry. *Phys. Rev. Lett.*, 100:013904, 2008.

[20] S. Raghu and F.D.M Haldane. Analogs of quantum-Hall-effect edges states in photonic crystals. *Phys. Rev. A*, 78:033834, 2008.

[21] M.C. Rechtsman, J.M. Zeuner, Y. Plotnik, Y. Lumer, S. Nolte, F. Dreisow, M. Segev, and A. Szameit. Photonic Floquet topological insulators. *Nature*, 496:196–200, 2013.

[22] K. G. Makris, S. Suntsov, D.N. Christodoulides, and G.I. Stegeman. Discrete surface solitons. *Opt. Lett.*, 30:2466–2468, 2005.

[23] M.I. Molina and Y.S. Kivshar. Discrete and surface solitons in photonic graphene nanoribbons. *Opt. Lett.*, 35:2895–2897, 2010.

[24] C. Kittel. *Introduction to Solid State Physics*. John Wiley & Sons, New York, NY, 1996.

[25] M. J. Ablowitz and Y. Zhu. Evolution of Bloch-mode envelopes in two-dimensional generalized honeycomb lattices. *Phys. Rev. A*, 82:013840, 2010.

[26] M.J. Ablowitz, C.W. Curtis, and Y. Zhu. On tight-binding approximations in optical lattices. *Stud. Appl. Math.*, 129:362–388, 2012.